Ceramics International 50 (2024) 50921–50933

Contents lists available at ScienceDirect

Ceramics International

journal homepage: www.elsevier.com/locate/ceramint

Limited dissolution of transition metals in the nanocrystalline cerium (IV) oxide

Agata Ducka [a,*], Patryk Błaszczak [a], Marcin Zając [b], Adrian Mizera [c], Francesco d'Acapito [d], Beata Bochentyn [a]

[a] Faculty of Applied Physics and Mathematics, Gdansk University of Technology, 80-233, Gdańsk, ul. Narutowicza 11/12, Poland
[b] National Synchrotron Radiation Centre SOLARIS, Jagiellonian University, Czerwone Maki 98, 30-392, Kraków, Poland
[c] Faculty of Materials Science and Ceramics, AGH University of Science and Technology, Al. A. Mickiewicza 30, 30-059, Kraków, Poland
[d] 2CNR-IOM-OGG c/o ESRF-The European Synchrotron, 71 Avenue des Martyrs, 38000, Grenoble, France

ARTICLE INFO

Handling Editor: Dr P. Vincenzini

Keywords:
Transition metal
Doped ceria
Reverse microemulsion method
Nanocrystallinity
Phase segregation

ABSTRACT

Nanocrystalline cerium (IV) oxides doped with transition metals have gained significant interest recently, mostly in the field of catalysis. Herein, we present the comprehensive studies on ceria doped with 10 mol.% of transition metals (Mn, Fe, Co, Ni or Cu) synthesized by the reverse microemulsion method. The aim of this work is to study the properties of those materials with the use of different complementary methods like XRD, SEM, TPR, and XPS and to determine the possibility of fabrication of single-phase materials with that doping level. Studies presented here prove that despite showing single-phase XRD patterns with high nanocrystallinity, in all obtained materials, the dopants are not fully incorporated in the ceria lattice. Spectroscopy studies show that additional transition metal oxides are present on the surface of all materials. Herein, we also present the analyses of $L_{3,2}$-edges of transition metals in ceria, as well as high energy Ce K-edge to prove that 10 mol.% of any of those transition metals cannot be incorporated in the ceria host without the formation of additional phases. Using techniques presented here, it was found that the highest share of Mn can be dissolved in the lattice, while Cu is mostly present as a surficial Cu_2O. Studies presented are an important contribution to the discussion about the solubility limits in nanocrystalline ceria and its properties which may be utilized for e.g various catalysts or as electrolytes.

1. Introduction

Cerium (IV) oxide (also known as ceria) is a rare-earth oxide that has attracted the most interest in various fields of material science. Among many applications, one may find gas sensors [1,2], electrolytes for Solid Oxide Cells [3–5], supercapacitors [6,7], or catalysts. For catalysis, it was utilized as a catalyst for soot combustion [8,9], CO [10–17], VOCs [18–20], and CH_4 oxidation [21–24] and water gas shift reaction [25–28], as well as photocatalysts [29–31]. Ceria owes its remarkable properties to the reversible transition between $Ce^{3+} \leftrightarrow Ce^{4+}$ oxidation states resulting in the high oxygen storage capacity and oxygen ionic conductivity [21,31–33]. It crystallizes in the fluorite structure with an energy band of ~3.2 eV [33,34].

The effectivity of CeO_2 used as a catalyst strongly relies on the surface morphology and specific surface area, thus synthesis of the nanoscaled materials is preferable. Several methods have been reported in the literature that allow the formation of nanomaterials with different morphology, however, most of them are wet chemistry methods [35–39].

One of the strategies to enhance the properties of the ceria is doping with different cations in the Ce sublattice [21]. Because other rare-earth metals are characterized by comparable ionic radii and similar available oxidation states, lanthanide doping is a common and successful approach fabricating single-phase materials [40–42]. For example, gadolinium-doped ceria (GDC) is commonly used as an electrolyte or buffer layer in Solid Oxide Cells [3,5,43,44]. Moreover, the transition metals were also reported to have a positive impact on the ceria properties, for example, doping with lower valence cations leads to the improved formation of oxygen vacancies, which influences oxygen storage capacity and O^{2-} mobility [21,45]. Those can also work as a sintering aid for easier CeO_2 densification [3]. Also, the addition of other cations may lead to synergistic effects as reported by Liu et al. [21] and Lee et al. [17] for the Mn-doped ceria. It is explained, by the favorable electron exchange between Mn and Ce ions leading e.g. to easier

* Corresponding author.
E-mail address: agata.ducka@pg.edu.pl (A. Ducka).

https://doi.org/10.1016/j.ceramint.2024.10.004
Received 3 July 2024; Received in revised form 17 September 2024; Accepted 1 October 2024
Available online 2 October 2024

reduction than each of the oxides themselves [21]. Lee et al. [17] suggested that lower valence cation doping and the introduction of multiple oxidation states ease the migration of O^{2-} ions through Mn-O bonds. Enhancement of the reducibility was also reported by Li et al. [46] for Fe-doping. However, they also stated that the solid solution of Ce-Fe-O is unstable at elevated temperatures, leading to the catalyst deactivation. Cobalt doping leads to a decrease in the ceria band gap and increased oxygen vacancy formation [37,47,48]. A similar effect on narrowing the band gap was observed for Ni doping, because it was found to form an additional impurity band just below the conduction band of the ceria, allowing the electron trapping [48]. Furthermore, incorporated nickel has a positive impact on redox properties of the compound by increasing the surficial reducibility compared to Ni nanoparticles precipitated on the ceria support [32]. Finally, the Cu is reported to decrease a redox potential due to the synergistic effect with $Ce^{4+/3+}$ redox couple [49]. Moreover, it was found that Cu^{2+} species are more active compared to CuO oxide and that more oxygen vacancies are formed around Cu^{2+} ions. Yang et al. [50] also found the preponderant existence of divalent cations which leads to the increased amount of lattice defects.

Generally, the solubility limit of transition metals in the ceria lattice is considered rather low [44], however, there is no agreement on the exact values and solubility can differ significantly across different works. For example, Kang et al. [51] stated that the solubility of Mn is located in the range between 5 and 10 mol.% and Mn_3O_4 mixed oxide is being formed above this limit. They have also pointed out that doping GDC with Mn may be much more difficult due to the formation of Mn-Gd mixed phases. This was confirmed by the work of Park et al. [4], in which the solubility limit was found to be even below 1 mol.% for Mn in the GDC. The solubility of the Fe is higher but also not consistent [52]. By the use of wet chemistry methods, the iron solubility was extended up to 15 mol.% [53], however those synthesis methods resulted mostly in nanocrystalline products. Saranya et al. [47] proved that 6 mol.% Co is the solubility limit of cobalt in the ceria lattice because for the higher quantities, additional CoO clusters were found. Other work [3] suggested that at high temperatures the solubility of Co would not exceed 3 mol.%. In the work by Rashid et al. [54] the Ni is found to have a solubility limit in ceria of 10–12 mol.%. Moreover, Derafa et al. [32] suggested that conventional catalysis preparation methods by e.g. co-precipitation do not provide homogenous dispersion of the dopant metal in the ceria host, which would further lead to the segregation of transition metal oxides. Simultaneously, another approach for the successful synthesis of single-phase material was proposed by using the Schiff base complexes for better dispersion [32]. Finally, several works on Cu-Ce-O systems proved that the maximum amount of fully soluble Cu that could form a solid solution is within 5–7.5 mol.% [49,55]. On the other hand, DFT + U calculations stand in opposition even to such small amounts, since no solid solution of Cu-Ce-O may be formed at equilibrium [56]. Experimental literature reports are in such cases explained as the non-equilibrium states.

Table 1 summarizes part of the literature reports on transition-metal doped ceria, including the doping level, synthesis method and discussed potential applications.

Table 1
Literature analysis of different transition metal-doped ceria.

Transition metal	Doping level	Synthesis method	Structure	Single phase	Application/study	Ref.
Mn	0.1–0.3 mol Mn:Ce	Thermal decomposition of metallic alkoxide precursors	Flower-like microstructures	Yes	CH_4 combustion	[21]
	0–3 mol.%	Solid state reaction	Pellets	Yes	Structural studies	[43]
Fe	2 mol.%	Co-precipitation	Nanocrystalline	Yes	Optical studies	[36]
	5, 10 mol.%	Solid state reaction	Not specified in the article	Yes	Structural, optical, and magnetic studies	[57]
	30 mol.%	Co-precipitation	Nanocrystalline	No[a]	CH4 oxidation	[24]
Co	2, 4, 7 mol.%	Co-precipitation	Nanocrystalline	Yes	Structural studies	[37]
	5 mol.%	Hydrothermal	Nanorods	Yes	Photodegradation of methylene blue	[48]
	3, 6 mol.%	Co-precipitation	Nanocrystalline	Yes	Photocatalysis	[47]
Ni	5 mol.%	Hydrothermal	Nanorods	Yes	Photodegradation of methylene blue	[48]
	2 mol.%	Co-precipitation	Nanocrystalline	Yes	Optical studies	[36]
	10 mol.%	Synthesis from Schiff base metal complexes	Nanocrystalline	Yes	Structural studies	[32]
	1, 3, 5 wt%	Biosynthesis	Nanocrystalline	Yes	Investigation of cytotoxic effect	[58]
Cu	5, 10, 20 mol.%	Reverse microemulsion method	Nanocrystalline	Yes	Structural studies	[38]
	10, 15, 20 mol.%	Urea-nitrate combustion method	Not specified in the article	Yes	CO oxidation	[12]
	1, 2, 5, 7, 10 mol.%	Urea precipitation	Microspheres	Yes	Photocatalysis	[29]
	<10 mol.%	Reverse microemulsion method	Nanocrystalline	Yes	Incineration of VOCs	[19,20]
	3, 5 mol.%	Solution combustion	Not specified in the article	Yes	Structural studies	[49]
	<15 mol.%	Self-propagating room temperature synthesis	Nanocrystalline	No[b]	Structural studies	[55]
	10 mol.%	Hydrothermal	Nanospheres	Yes	CO oxidation	[50]
Mn, Fe, Co, Ni, Cu	10 mol.%	Co-precipitation	Nanocrystalline	No, for Ni and Co Yes, for Mn, Fe, and Cu	Thermochemical CO_2 splitting	[59]
	10 mol.%	Hydrothermal	Nanocrystalline	No, for Fe, Co, Ni Yes, for Cu and Mn	Toluene oxidation	[45]
	10 mol.%	Pyrolysis of bimetallic coordination polymers	Hierarchical nanoporous structures	Yes	CO oxidation	[17]
	20 mol.%	Reverse microemulsion method	Nanocrystalline layers	No, for Co Yes, for Mn, Fe, Ni, Cu	Layers for DIR-SOFC	[60]

[a] additional α-Fe_2O_3 present on the surface.
[b] copper segregation on the crystallite surfaces.

As presented in Table 1, the synthesis of nanocrystalline CeO_2 and its doping with the transition metals have been extensively studied in recent years for different purposes. Before, we have synthesized ceria layers doped with transition metals for DIR-SOFCs [60]. In that work, the enhanced stability of Ni- and Co-doped samples in biogas was reported, but the nature of this superiority was not clear. Moreover, it was not clear whether the transition metals were fully incorporated into the lattice. In the literature, several different methods have been utilized for the characterization of transition metals-doped ceria and among them XRD, SEM, TPR, and XPS remain the most popular [32,33,51,53,61]. At the same time, only several studies [15,62–64] show the X-ray absorption spectroscopy to be used to probe the properties of ceria doped with transition metals. Moreover, in those studies, the focus is put on the K-edge of respective transition metals, while $L_{3,2}$-edges are highly underrecognized in those systems. The work of Kumar et al. [63] focused on the XAFS analysis of Co-doped ceria but the maximum Co loading was 7 mol.% and they have found that the Co has been incorporated into the lattice.

Herein, we present the comprehensive characterization of the nanocrystalline ceria doped with 10 mol.% of transition metals. We've used interdependent techniques like XRD, SEM, FTIR, XPS to understand more the cerium (IV) oxides properties. Lastly, we've utilized soft and hard X-rays to probe $L_{3,2}$-edges of transition metals and K-edge of cerium, respectively. The use of Wavelet Transform of Ce K-edge allowed us to image cerium shells. We believe that comprehensive analyses presented in this work, will be of significant contribution to understanding ceria properties and to the discussion on the transition metals' solubility limits in ceria lattice.

2. Experimental

2.1. Synthesis of nanocrystalline ceria doped with transition metals

Cerium (IV) oxides doped with 10 mol.% transition metals, namely $Ce_{0.9}M_{0.1}O_{2-\delta}$ (M = Mn, Fe, Co, Ni, Cu) were synthesized using the reverse microemulsion method. The synthesis method was based on [60] with small adjustments regarding the solvents used for rinsing. All reagents used for the synthesis were of analytical grade and purchased from Chempur (solvents) or Sigma-Aldrich (nitrates: $Mn(NO_3)_2 \bullet 4H_2O$, $Fe(NO_3)_3 \bullet 9H_2O$, $Co(NO_3)_2 \bullet 6H_2O$, $Ni(NO_3)_2 \bullet 6H_2O$, $Cu(NO_3)_2 \bullet 3H_2O$, min. 99.9 % purity). The stoichiometric amounts of metal nitrates were dissolved in DI at RT, while in another beaker a solution of cyclohexane, pentan-1-ol, and Triton X-100 was prepared. Firstly, the nitrate solution was added to the organic solvents, and then tetramethylammonium hydroxide (TMAOH) was added, which resulted in immediate precipitation of the product. The mixture obtained was stirred for approximately 30 min, and then the precipitate was separated by decantation. The residual organic solvents were further separated by the centrifuge rotating at 4500 RPM for 8 min. To provide high purity of the material and to ensure that all solvents were removed, the centrifugation step was repeated four times, and after each step, the precipitates were additionally rinsed with acetone (twice) and isopropanol (twice). The remaining gel was put into the alumina crucible and dried overnight at 80 °C. The dried material was then fired in the air at 500 °C for 2 h to remove any residual organic compounds. To determine the phase transition after the recrystallization, the samples of synthesized powders were additionally annealed in air at moderate temperature (800 °C) for another 2 h. This enabled the growth of the crystallites which allowed for proper phase characterization.

2.2. Characterization methods

The diffraction patterns of the as-synthesized and annealed at 800 °C powders were collected at room temperature using Bruker D2 PHASER XE-T with Cu-Kα radiation source. HighScore Plus 3.0.2 software from PANalytican was used to analyze obtained diffraction patterns.

The average crystallite size in as-synthesized and annealed states was calculated based on the Scherrer formula. In order to determine the phase composition of the samples and unit cell parameters of ceria, the Rietveld refinement was performed on annealed oxides. It was due to satisfactory reading intensity in contrast to as-synthesized powders.

The microstructure and morphology of investigated materials were revealed using the Scanning Electron Microscope (SEM, FEI Quanta FEG 250) with a secondary electron detector operating under high vacuum conditions with an acceleration voltage of 10 kV. A quantitative elemental composition analysis was performed using Phenom XL desktop microscope (Thermo Fisher Scientific, The Netherlands) with the EDS spectroscopy analyzer (Thermo Fisher Scientific, 25 mm^2 Silicon Drift Detector).

The Temperature Programmed Reduction (TPR) and Temperature Programmed Oxidation (TPO) tests were carried out in AutoChem II 2920 (Micromeritics, TCD detector) under 40 mL min^{-1} stream of 5 % v/v H_2 in Ar and 2 % v/v O_2 in Ar, respectively. The tests were carried out from 100 °C to 700 °C with a heating rate of 10 °C min^{-1}. Two reduction cycles with the collection of oxidation profile were performed each time to deliver more reliable data and to reveal the possible changes in the materials.

To determine the presence of different functional groups in doped CeO_2, Fourier transform infrared (FTIR) spectroscopy measurements were performed on the Perkin-Elmer Frontier MIR/FIR spectrometer with a TGS detector. Data was collected on pellets mixed with potassium bromide (KBr) in a weight ratio1:100. In order to analyze the recrystallization process and to reveal its temperature range, a differential scanning calorimetry (DSC) using Netzsch Thermal Analyzer DSC 204 F^1 Phoenix was utilized. Each powder (~5 mg) was put into an aluminum crucible and measurements were carried out in synthetic air with a heating rate of 10 °C min^{-1} in 35–600 °C range.

X-ray Photoelectron Spectroscopy (XPS) spectra were collected using Omnicron NanoTechnology X-ray photoelectron spectrometer with 128-channel collector. XPS measurements were performed under ultra-high vacuum conditions, below $1.1 \bullet 10^{-8}$ mbar. The photoelectrons were excited by an Mg-Kα X-ray source with the anode operating at 15 keV and 300 W. The obtained spectra were deconvoluted using XPSPEAK41 freeware software.

X-ray absorption spectroscopy (XAS) measurements were performed at both the SOLARIS National Synchrotron Radiation Center in Kraków (Poland) and LISA beamline at the European Synchrotron Radiation Facility in Grenoble (France). Measurements at SOLARIS allowed to collect $L_{3,2}$ edges of transition metals, K-edge of oxygen and M-edge of cerium. Well-ground powders were evenly distributed on the carbon tape and then placed on a standard flag-style sample holder. The measurements were performed at room temperature under ultra-high vacuum using total electron yield (TEY) mode. Spectra were normalized using PyMca software and analyzed by comparison to reference oxides spectra collected under the same conditions. Hard X-rays were utilized to collect Ce K-edge at LISA beamline at ESRF [65]. The appropriate amount of finely ground powder was mixed with ethylcellulose and pelletized. All spectra were collected in transmission mode with the samples cooled using liquid nitrogen to hinder thermal fluctuations. Athena software was utilized to normalize the spectra, as well as to perform Fourier transform analysis of EXAFS. For the Fourier transform only the wave number k in the range 3–13 $Å^{-1}$ was taken into account, which is comparable to reports from the literature [66]. Finally, the phase correction of 0.5 Å was applied. Wavelet transform was performed in the Fastosh freeware software (ver. 1.0.7.2) in the same wave number regime as the Fourier Transform. For the analysis $\eta = 7.5$ and $\sigma = 1$ were used as parameters for Morlet Wavelet transform.

3. Results

3.1. Phase composition and microstructure of the materials

The phase composition of as-synthesized nanocrystalline oxides, as well as recrystallized powders after additional annealing, was determined using the XRD method and can be found in Fig. 1. All peaks detected for as-synthesized oxides can be attributed to the fluorite (*Fm-3m*) structure of the cerium (IV) oxide and all detected planes are denoted with their Miller indices. Prepared powders were characterized by high nanocrystallinity and/or high strain, which was testified by broad XRD peaks. In order to determine mean crystallite size, the Scherrer equation was utilized and results are presented in Table 2. No additional peaks other than CeO_2 fluorite phase were found in XRD pattern of as-synthesized powders, however, the intensity of the signal was quite low and other phases might be below the instrument detection limits or lost within the noise. Some papers [45,67,68] suggested that in similar cases oxides may be present as highly dispersed clusters on the surface or in the amorphous state, which would make them invisible in XRD pattern. In such case, the material could be undoubtedly considered as single-phase only when no additional phases would be observed after thermal treatment. Thus, to determine whether new diffraction peaks would appear after recrystallization, the annealing process was performed, allowing also to perform reliable Rietveld refinement. Obtained XRD patterns are presented on the right in Fig. 1. One may notice that ceria remains the main phase present in all powders with a significant decrease in FWHM. This implies crystallite growth even after short exposition to elevated temperatures. Not only the peaks got narrower, but also additional small peaks from respective oxides have been found after the annealing in all of the transition metal-doped cerium (IV) oxides. The amount of additional oxides and the ceria unit cell parameter of each sample were calculated using Rietveld refinement, and the results are presented in Table 2. In the literature, there is no absolute agreement on the amount of transition metals that can be incorporated into the ceria lattice without the formation of secondary phases. Some studies show that the solubility limit is low, and then doped metals would rather form new phases mostly on the grain boundaries or forming core-shell structures [44,56,69], while others state that the synthesis of single-phase ceria doped with ≥10 mol.% of transition metals is possible, mostly in nanocrystalline cerium (IV) oxide [17,20,46,55,60]. Studies presented here show that the presence of transition metals in CeO_2 is hindered by nanocrystallinity in as-synthesized compounds and additional phases are visible after crystallization of the powders. Another possibility is that the dopants are present in a metastable state and upon heat treatment form their respective oxides on the grain boundaries, as suggested by Avila-Paredes et al. [69].

Almost all doped oxides exhibit smaller unit cell parameter compared to pristine ceria, which could be considered as an indicator of partial dissolution of the transition metals in the CeO_2 lattice. The shrinkage of the unit cell results from smaller ionic radii of the transition metals (Mn^{2+}: 0.96 Å, Mn^{3+}: 0.645 Å, Fe^{2+}: 0.92 Å, Fe^{3+}: 0.78 Å, Co^{2+}: 0.9 Å, Co^{3+}: 0.61 Å, Ni^{2+}:0.69 Å, Ni^{3+}: 0.6 Å, Cu^{+}: 0.77 Å, and Cu^{2+}: 0.73 Å) than Ce^{4+} (0.97 Å) [70]. However, not only do the ionic radii of the implemented dopant play a crucial role in the resultant lattice constant of synthesized oxides. The other aspects that should be considered are the amount of Ce^{3+}, which has a larger ionic radius (1.14 Å) and/or the formation of the oxygen vacancies, also leading to the expansion of the unit cell. Expansion of the unit cell was observed only for Co-doped ceria, suggesting enhanced formation of Ce^{3+} ions, oxygen vacancies, or interstitial defects of Co^{x+}. Dziembaj et al. [20] explained the ceria unit cell expansion in terms of the formation of oxygen vacancies and structural distortions. Similarly, here, the distortion would originate from an unusual coordination number (CN = 8) for Co^{x+} ions, after possible incorporation into the ceria lattice. Kurajica et al. [45] have fairly pointed out that the analysis of the unit cell parameter only cannot be taken as direct proof of the successful incorporation of other ions into the host ceria and formation of the solid solution. All variables mentioned above may lead either to the expansion or the shrinkage of the unit cell, and it is impossible to unambiguously state which one is dominant without additional analyses.

The structure of nanocrystalline as-prepared ceria doped with different transition metals was revealed by SEM imaging. Corresponding micrographs are presented in Fig. 2. There was no clear microstructural difference found between each dopant. All the compounds show agglomerates with subgrains of nanometer size. Several other studies have shown that nanocrystalline ceria (with grains <10 nm) tends to aggregate into larger structures, without the correlation with the type of dopant to be incorporated into the lattice [37,39,42,71–73]. Obtained structures look much like agglomerates obtained by the reverse microemulsion method by Paschalidou et al. [39], proving that this method allows for the synthesis of replicable nanostructures. The exact size determination of nanograins is beyond the resolution of SEM imaging, however, it is clearly visible that the crystallite sizes were found to be in a similar range in comparison to the XRD results for as-synthesized oxides, which was discussed in more detail above. To reveal possible phase separation in transition metal doped CeO_2 imaging in BSE mode was also used. The images were collected for the as-synthesized powders immersed in the epoxy resin, which was further finely polished. The

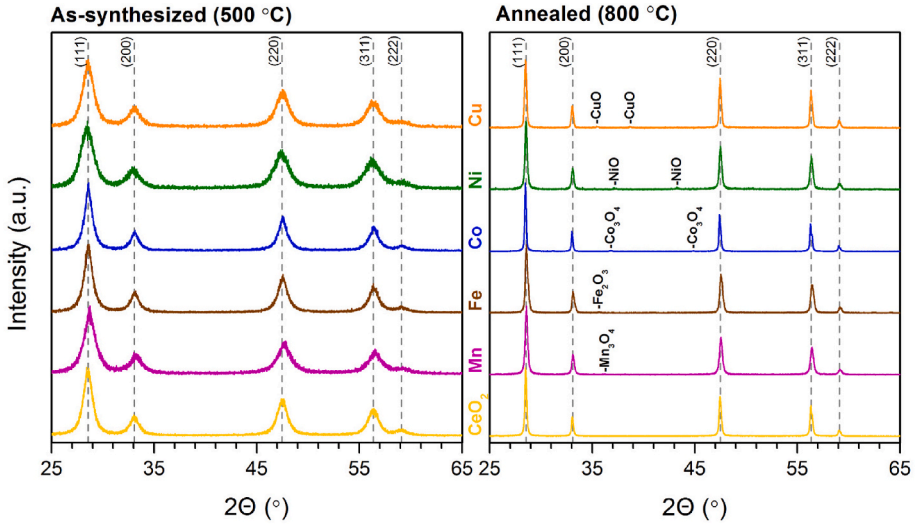

Fig. 1. XRD patterns for doped ceria after synthesis (left) and after additional heat treatment at 800 °C (right).

Table 2
Average crystallite size in as-synthesized oxides calculated from Scherrer equation and results of Rietveld refinement on annealed ones.

Nominal composition	$CeO_{2-\delta}$	$Ce_{0.9}Mn_{0.1}O_{2-\delta}$	$Ce_{0.9}Fe_{0.1}O_{2-\delta}$	$Ce_{0.9}Co_{0.1}O_{2-\delta}$	$Ce_{0.9}Ni_{0.1}O_{2-\delta}$	$Ce_{0.9}Cu_{0.1}O_{2-\delta}$
As-synthesized						
Average crystallite size (nm)	7.5 ± 0.5	5.7 ± 0.3	8.4 ± 0.5	6.1 ± 0.3	5.1 ± 0.7	9.1 ± 0.7
Annealed						
Phase composition (wt.%)	CeO_2: 100	CeO_2: 98 Mn_3O_4: 2	CeO_2: 96.5 Fe_2O_3: 3.5	CeO_2: 95.8 Co_3O_4: 4.2	CeO_2: 96.3 NiO: 3.7	CeO_2: 96 CuO: 4
a_{CeO2} (Å)	5.4091(1)	5.4081(2)	5.4088(1)	5.4110(1)	5.4082(1)	5.4077(1)
Goodness of fit (GOF)	1.88	1.28	1.57	1.44	1.57	1.83

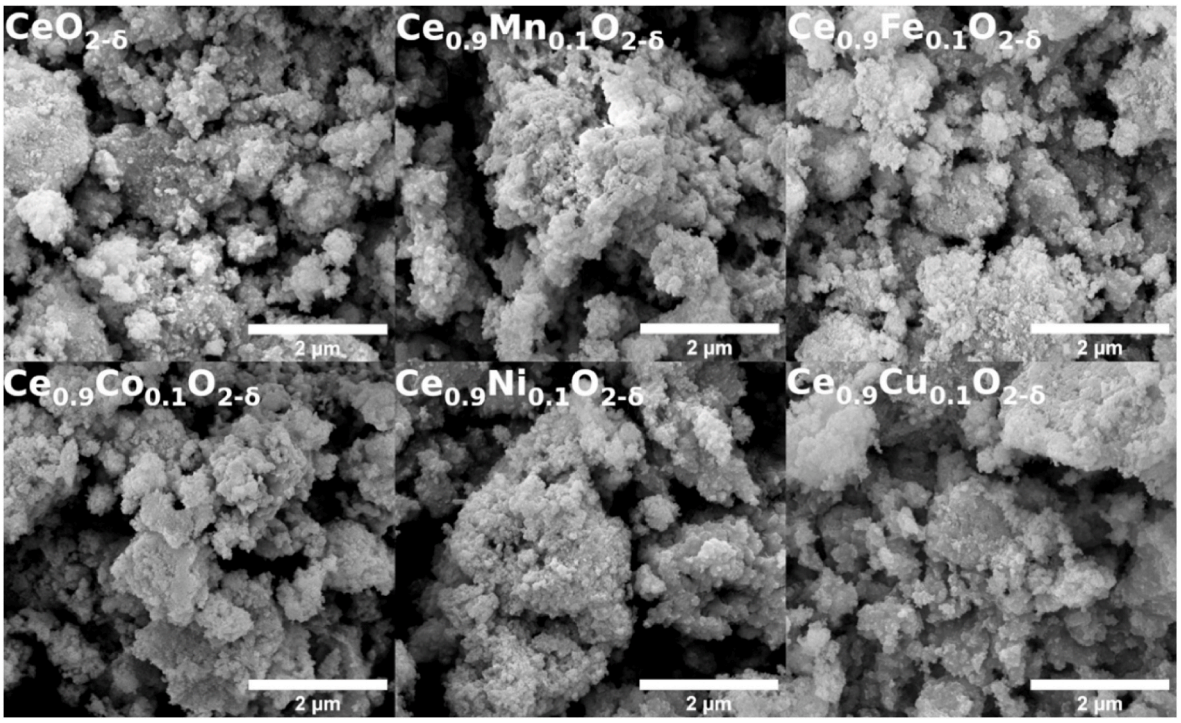

Fig. 2. SEM micrographs of nanocrystalline as-prepared ceria with different dopants. Images were taken in secondary electrons detection mode.

images taken in BSE (back-scattered electron) mode are shown in Fig. S1 in the Supplementary Materials. It is clearly visible that for all the synthesized oxides, micrometric segregation occurs. Interestingly, it was the most visible for the Mn- and Fe-doped ceria, which were characterized by the lowest amount of additional oxides after the reoxidation. This suggests that even before thermal treatment, some amount of transition metal oxides was already present on the surface and the metals have not been fully incorporated into the lattice as planned during the synthesis.

Powders submerged in the epoxy resin were also investigated by means of the EDS analysis. Spectra collection on the selected grains allowed to calculate the relative molar concentration of cerium and each of the transition metals. Due to the limitation of the EDS method, oxygen was not taken into consideration. The amount of transition metals was found to be: 10.5 mol.% for Mn-, 12.5mol.% for Fe-, 9.1 mol.% for Co-, 9 mol.% for Ni-, and 10.7 mol.% for Cu-doped ceria. The results are burdened with 0.5 mol.% uncertainty. Obtained amounts were close to the nominal; however, it cannot be sufficient to determine whether the metals are incorporated into the bulk of the ceria. At the same time, the ratio between Ce and the transition metals being close to the nominal values may suggest that even if the metals remain as additional phases on the surface, they are rather evenly distributed in synthesized powders. In the case of Fe-doped sample, the increase in the overall content of Fe may suggest the presence of Fe-enriched areas in the sample.

3.2. *Temperature programmed reduction*

All as-synthesized powders underwent temperature programmed reduction (TPR) measurements to reveal their reductivity and to analyze the behavior of additional species present in the lattice and/or as secondary phases, which might not have been identified in earlier studies. Before testing, powders were degassed under flowing He at 200 °C for 1h. Two reduction runs were performed with intermittent temperature-programmed oxidation (TPO) to reveal metals' stability and/or agglomeration tendency. The O_2-TPO profiles are presented in Figs. S2–B. The H_2-TPR profiles for two reduction cycles were normalized to 1 and are presented in Fig. 3. For the pristine CeO_2 in the analyzed temperature range one main peak may be found at around 524 °C, which is widely reported in the literature [74–76] as surface reduction of Ce^{4+} to Ce^{3+}. In addition to the main peak of surface reduction, a smaller one can be observed on the lower temperature side. Qi et al. [29] suggested that such a maximum may originate from the hydroxyl groups on the ceria surface which would be reduced according to the equation: $2Ce^{4+} + 2OH^- + H_2 \rightarrow 2Ce^{3+} + 2H_2O$. For the doped compounds, the consumption peak for pure ceria was overwhelmed by the much more intense peaks from respective transition metals. The TCD signal without normalization is presented in Fig. S2-A and S2-C, where it can be seen that signal from pristine ceria is weaker than other metals.

Taking into account the Mn-doped sample, for the first reduction cycle, one sharp peak is located at 275 °C followed by a plateau up to

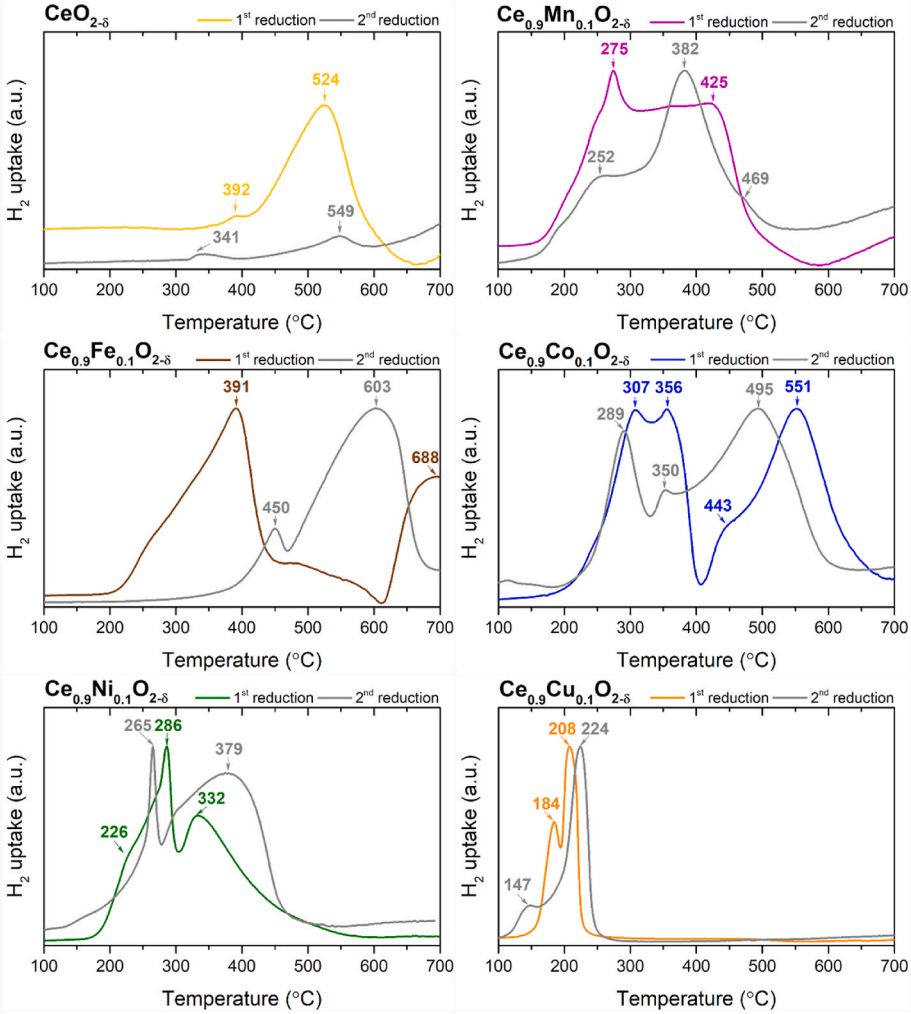

Fig. 3. TPR profiles for two reduction cycles for transition metal doped cerium (IV) oxide.

425 °C. The first one originates from the reduction of MnO_2 and Mn_2O_3 oxides with low crystallinity, well dispersed on the surface [17]. The higher temperature plateau consists of the overlapping peaks from the subsequent reduction from Mn_2O_3 to Mn_3O_4 mixed oxide and finally to MnO at higher temperatures [77]. Lee et al. [17] have reported a similar TPR signal as presented herein, however, they have noticed an additional low-temperature peak. Its formation has been explained by the dispersion of Mn ions in the lattice and the creation of a solid solution. Herein, as no such peak is observed even for comparable metal doping, one may deduce that manganese was not fully incorporated to form a solid solution and is present as oxides dispersed on the surface. The second reduction cycle differs significantly, and two distinguishable peaks are found: one at 252 °C. and the latter, a bigger one at 382 °C. The shape of TPR profile for the second reduction is similar to the typical for MnO_2 [77], yet the peak temperature is slightly lower than the literature [18,78]. Moreover, the bigger Mn_3O_4 agglomerates are still present on the surface, as indicated by overlapping small peaks at 469 °C [77].

The TPR profile of Fe-doped sample consisted of two separated consumption peaks that could be found in both reduction cycles. In the first reduction profile, peaks are found at 391 °C and 688 °C. The first reduction profile resembles the one obtained by Li et al. [46]. The peaks may be identified as the reduction of free Fe_2O_3 particles to Fe_3O_4 and subsequently to metallic iron [8,79]. The second reduction profile exactly matches the one reported in Ref. [77] for impregnated nanocrystalline ceria with surficial Fe clusters. Such observation confirms that non-incorporated iron is agglomerating on the surface. Herein, the consumption peak centered at 450 °C is associated with the reduction of Fe_2O_3 to Fe_3O_4 and then the reduction to FeO and Fe^0 is visible as the peak at 603 °C.

Considering Co-doped ceria, in both the first and second reduction cycles, the TPR profile can be divided into two regions, low temperature one up to c.a. 400 °C and the second up to 600 °C. For initial reduction, the low-temperature reduction range shows two distinguishable peaks of comparable intensity at 307 °C and 356 °C. Low-temperature regime results from the reduction of loosely integrated cobalt ions while the high one is the reduction of the ones strongly coupled with the CeO_2 [77]. Furthermore, lower temperature peaks can be assigned as the reduction of Co^{3+} to Co^{2+} and then Co^0 as temperature increases [8,10,80]. The slightly lower reduction temperatures when compared to Co_3O_4 originate from the presence of finely dispersed Co-species on the ceria surface [61].

The Ni-doped CeO_2 exhibited two peaks: a sharp one at lower temperature (250–300 °C) and a much wider one between 330 and 400 °C. Additionally, for the first reduction cycle, a small consumption peak is formed at even lower temperatures (~225 °C). The sharp consumption peak at lower temperatures originates from the reduction of the NiO surficial nanoparticles [22,77], while the broad one at higher temperatures results from the reduction of the NiO species strongly interacting with CeO_2 support [22,54]. The presence of a second reduction peak thus can be considered as an indicator of the strong interaction between metal and the support by the Ce-Ni-O solid solution interlayer [77].

Unlike other analyzed materials, the reduction of Cu-doped ceria is

completed up to 250 °C in both reduction cycles. The first profile is characterized by two overlaying peaks centered at 184 °C and 208 °C, respectively, while for the second reduction run, the peaks are more separated and located at 147 °C and 224 °C. Razegi et al. [76] stated that the first reduction peak originated from the reduction of finely dispersed CuO clusters and the latter one from the reduction of the CuO bulk phase. The paper of Yang et al. [50] agreed on the origin of the first peak, however, the second is explained by the reduction of Cu^{x+} in the form of substitutional defects in the CeO_2 host lattice. The peak temperatures for both reduction processes are relevantly lower than those for pure CuO oxide [50,68]. This behavior confirms the formation of nano-sized Cu_xO species finely dispersed on the surface [77]. Comparable peak temperatures were shown by Tang et al. [11] for the CuO (5 wt.%) deposited on the ceria support as an additional phase. This is another evidence of the formation of a Cu-rich secondary phase rather than the formation of a solid solution.

The lack of reproducibility as seen by changes in first in second reduction profiles for all samples arises from the irreversible morphology changes e.g., re-distribution or agglomeration [11]. As a summary for TPR measurements, one may state that dopants tend to form surficial dopants interacting with ceria support. The aforementioned results confirm that 10 mol.% of dopants loading in ceria is above the solubility limit of those metals in cerium (IV) oxide, even in the nanocrystalline form.

3.3. FTIR and DSC analysis

The FTIR spectra for undoped and transition metal-doped CeO_2 are plotted in Fig. 4 on the left. All compounds are characterized with the same bands, and their wavenumbers are marked at the bottom of the graph. Most of the identified bands originated from species adsorbed on the ceria surface like water, carbon dioxide, or organic residuals. Several bands overlap and could be identified as originating either from ceria or CO_2. The presence of the peak at 850 cm^{-1} could be identified in two ways: as the bending mode of Ce-O [7,81] or the bending vibrations of CO_3^{2-} [36]. Muduli et al. [7] suggested that the presence of the band at 850 cm^{-1} confirms the presence of ceria without impurities. Also, the peak at 1385 cm^{-1} may be associated with CeO_2, however, it overlaps with other bands like COO, Ce-O-C or Ce-O-H stretching modes [39]. Wide bands at 3421 cm^{-1} originate from water physically absorbed on the ceria surface, and more specifically from O-H symmetric stretching vibration [7,73,82]. Furthermore, bending vibrations of H-O-H from the physiosorbed water can be found at 1636 cm^{-1} [6,82]. Other bands associated with the presence of CO_2 on the surface are one at 1060 cm^{-1} which could be identified as stretching vibrations of C-O and the second seen as a wide band between 1539 and 1636 cm^{-1} being stretching band of O-C-O, overlapping with H-O-H bending ones [71]. A band located at 1322 cm^{-1} might arise from the presence of residual organics on the surface [78].

Considering that after the annealing, the crystallinity of the oxides increased, DSC studies were performed to reveal thermodynamic processes happening in the samples. Interestingly, no sharp peaks were found for all doped compounds (see the graphs in Fig. S3 – Supplementary Materials), only for Fe-doped one, a small maximum is formed at around 180 °C. For the pristine ceria, an exothermic peak is formed at 173.7 °C followed by a significantly smaller one at 278.9 °C. The analogous exothermic peak was found in the paper of Paschalidou et al. [39], who synthesized ceria using the Triton-X-based reverse microemulsion method. Although the origin of such a peak was not explained in detail, it can be concluded that it originates from the decomposition of Triton-X surfactant. The other peak is attributed to the decomposition of the remaining organic residuals and/or cerium oxidation, as suggested by Choolaei et al. [5]. Because such peaks are visible mostly for pristine ceria, this suggests that for the undoped sample, some of the organic residuals remain even after a short thermal treatment at 500 °C. This may be explained by the slightly increased quantity of organic reactants and solvents remaining in the oxide, which were not sufficiently removed during decantation, centrifugation, and burnout.

3.4. The investigation of metals' valence state by XPS and XAS studies

To reveal the valence state of the transition metals in the surface layers of doped ceria, X-Ray Photoelectron Spectroscopy was utilized to collect the spectra of 2p levels of the transition metals and 3d level of cerium. Fig. 5 represents the Ce 3d spectra for the pristine, undoped oxide with 5 fitted spin-orbit doublets. The peaks of Ce $3d_{3/2}$ were denoted with *u*, while *v* was used for $3d_{5/2}$ peaks. Proper determination of the valence state in cerium is very complex due to complicated valence and core electron spectra [83,84]. The doublet *u (v)* originates from the Ce^{4+} ground Ce $3d^94f^2$ O $2p^4$ final state, while *u'(v')* and *u'''(v''')* were associated with excited states: Ce $3d^94f^1$ O $2p^5$ (charge

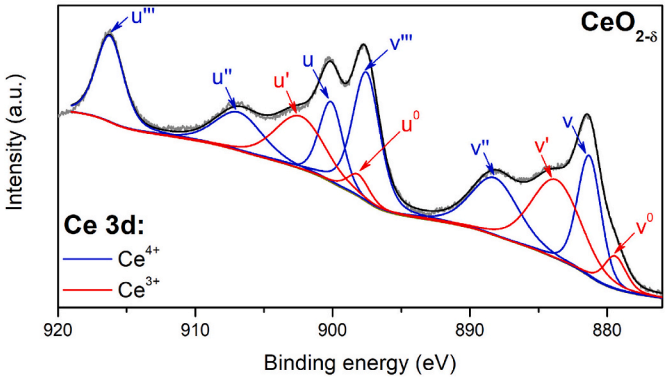

Fig. 5. Ce 3d XPS spectra collected for undoped ceria.

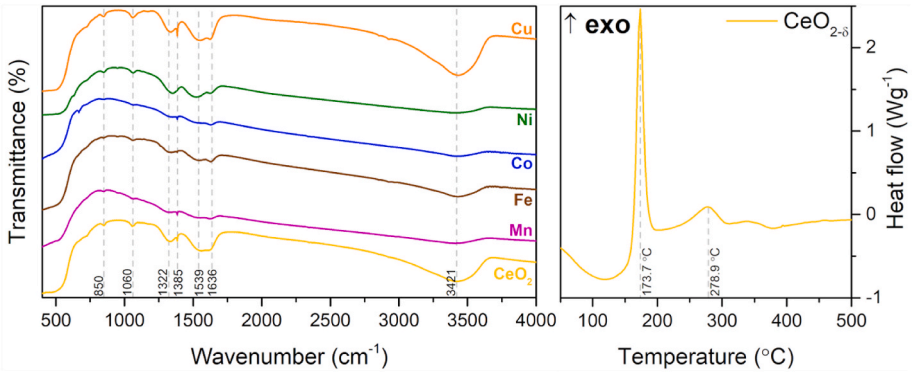

Fig. 4. FTIR spectra of as-synthesized oxides (left) and DSC signal for pristine CeO_2 (right).

transfer satellites) and Ce $3d^94f^0$ O $2p^6$ (shake-up satellites), respectively [57,85]. The Ce^{3+} final states (Ce $3d^94f^1$ O $2p^6$) and (Ce $3d^94f^2$ O $2p^5$) were denoted as v^0 (u^0) and v' (u') respectively [85]. The Ce 3d fitted spectra in other samples are presented in Fig. S4. Although, all doped compounds exhibit 5 doublets, the area of respective pairs slightly differs between all of them, which allowed for the calculation of the mean oxidation state of cerium ions.

The values calculated for transition-doped ceria are presented in Table 3, as well as the calculated mean valence state of cerium. Generally, the doping has increased the amount of Ce^{4+} ions in all oxides compared to pristine ceria. Such behavior indicates that the transition metal cations in doped material are present in a lower valence state (e.g., $Mn^{2+/3+}$ rather than Mn^{4+}). The analysis of the valence state of respective transition metals by means of XPS and XAS studies will be discussed in more detail in the following part of the manuscript. Because the electroneutrality of the compound must be preserved, the incorporation of the lower valence cations will either lead to the formation of the oxygen vacancies or an increase in the amount of Ce^{4+} ions. Soni et al. [57] have also observed the changes in the Ce valence state, however, when the doping increased, the amount of Ce^{4+} decreased which is contrary to the aforementioned results. Such opposite behavior was explained by the enhanced formation of the oxygen vacancies, guaranteeing the electroneutrality of compounds. On the other hand, the paper of Li et al. [46] on Fe-doped ceria with even higher dopant loading (20 mol.%), has shown that more Ce^{4+} was formed. Furthermore, in their work, they have suggested that the presence of Ce^{3+} cations may be considered as an indicator of oxygen vacancies. This being said, transition metal doping in the microemulsion-derived ceria suppresses the formation of oxygen vacancies. Wu et al. [86] in their paper on heavily Mn-doped have found that the Ce^{4+} amount increases with increasing doping level due to the electron transfer from Ce^{4+} to Mn^{x+}, thus manganese is expected to be in lower valence states.

The XPS spectra for respective dopants are presented in Fig. 6. For the nickel spectrum, only the Ni $2p_{3/2}$ peak is shown, due to the $2p_{1/2}$ level overlapping with a much stronger Ce 3d signal [32]. For other metals, both $2p_{1/2}$ and $2p_{3/2}$ were fitted. Due to the small concentration of the dopants in the ceria, signal to noise ratio is higher than for Ce 3d spectra, especially for the Co-doped CeO_2. Thus, the amount of transition metals calculated from the fitting is burdened with significant uncertainty (~5 %) and presented in Table 3. The spectra of all analyzed compounds could be deconvoluted into distinguishable doublets and satellite peaks, meaning that metal cations are present in mixed-valence state. For all the dopants considered, cations are present mostly in their lower valence states, with nickel being the only exception from this observation. Thus, Mn, Fe, and Co can be found predominantly in 2+ state, copper in 1+, and nickel in 3+. Considering the Mn-doped sample, three different states of Mn were recognized with the highest contribution from Mn^{2+} ions, while the amount of Mn^{4+} is the lowest. The $2p_{3/2}$ peaks were found at 639.21 eV, 640.47 eV and 642.8 eV for Mn^{2+}, Mn^{3+} and Mn^{4+} respectively. The spin-orbit splitting was found to be equal to 11.6 eV (Mn^{2+}), 11.8 eV (Mn^{3+}) and 11.9 eV (Mn^{4+}). Distinguished peaks for the Fe-doped compound originated from Fe^{2+} and Fe^{3+} ions with the spin-orbit splitting energy equal to 13.6 eV and were found at 710.22 eV (Fe^{2+}) and 712.12 eV (Fe^{3+}). For Co-doped sample, 2p spectrum was deconvoluted into two distinguishable doublets: from Co^{2+} and Co^{3+} located at 780.34 eV and 779.27 eV, respectively. Splitting energies for those two peaks were found to be 15.6 eV (Co^{2+}) and 15.3 eV (Co^{3+}). The spectrum is dominated by the highest share (85 %) of Co^{2+}ions. This observation agrees with the study by Kumar et al. [63] in which they analyzed the EXAFS spectrum and found that Co^{2+} is predominant cation being substituted at the Ce sites. The detected spectrum for Ni $2p_{3/2}$ was deconvoluted into Ni^{2+} and Ni^{3+} peaks, found at 854.23 eV and 855.51 eV, respectively. The predominant presence of trivalent Ni cations agrees with other studies on $Ni_{0.1}Ce_{0.9}O_{2-\delta}$ indicating partial incorporation of nickel into the ceria lattice [32]. The simultaneous existence of Ni^{2+} originates from bulk NiO agglomerates on the surface. The Cu 2p spectrum is dominated by an intense Cu^{+} peak at 930.93 eV ($2p_{3/2}$) with 19.8 eV doublet separation energy, however also a small Cu^{2+} peak ($2p_{3/2}$ at 933.75 eV with spin-doublet splitting of 20 eV) was recognized. Another clear evidence of the predominant presence of Cu^{+} is an extremely weak shake-up satellite, which was already associated with the presence of lower valence of copper in ceria by other research groups [12,14]. The preferred formation of 1+ valence state is explained by the bigger ionic radii of Cu^{+} rather than Cu^{2+}, thus it may be more easily incorporated into the ceria lattice [12]. Papers by Tschope et al. [68] and Avgouropoulos et al. [67] suggested that the presence of Cu^{+} originates from Cu_2O clusters on the surface, strongly interacting with cerium (IV) oxide.

In addition to XPS studies, the X-Ray Absorption Spectroscopy (XAS) technique was used to further help in the proper determination of the valence states in the compounds. The normalized $L_{3,2}$-edge spectra of both as-synthesized (solid line) and annealed (dashed line) samples are plotted in Fig. 7. Additionally, selected reference oxides' spectra were added. Spectra before and after the annealing differ significantly, which is direct proof that oxides visible in XRD patterns were crystallized during the annealing process rather than being already present after the synthesis. This is another evidence for the existence of the clusters of the oxides in the ceria matrix, which was suggested in a discussion of the results of TRP and XPS.

The spectra of as-synthesized oxides are a superposition of spectra from respective oxides, whose presence was also deducted from XPS studies. The Mn-doping results in a formation of mostly Mn^{2+} with a small addition of Mn^{3+}. A slight amount of Mn^{4+} can also be found, indicated by a small peak at 644 eV. After the annealing, the ions were oxidized mostly to Mn_3O_4 and MnO_2, agreeing with the XRD observations. The proper identification of Fe valence state from the XAS spectra is not trivial. This is because of the similarities in the $L_{3,2}$ spectra of all reference oxides. Both spectra before and after annealing have a similar shape, yet the peaks' normalized intensity was influenced. Considering the intensity ratio of two L_3 peaks and the formation of pre-peak at 706 eV, it can be stated that most iron is present in 2+ state. This observation is consistent with the XPS findings, while for the annealed sample, the most probable is oxidation to Fe_2O_3 or mixed Fe_3O_4 oxides. The Co-doped ceria is as-synthesized and can also be considered as a superposition of CoO and Co_3O_4. The additional heat treatment results in oxidation of all cobalt purely to Co_3O_4. The Ni L-edge for as-synthesized compound consists of two contributions: from Ni^{2+} and Ni^{3+}. The presence of Ni^{3+} cations was recognized by the odd shape of Ni L-edge spectra and by the comparative studies with $LaNiO_3$ reference. Unfortunately, the $LaNiO_3$ reference spectrum is overwhelmed by the La M_4

Table 3
Mean valence state of cerium and respective transition metals calculated from XPS analysis.

	Nominal composition	$CeO_{2-\delta}$	$Ce_{0.9}Mn_{0.1}O_{2-\delta}$	$Ce_{0.9}Fe_{0.1}O_{2-\delta}$	$Ce_{0.9}Co_{0.1}O_{2-\delta}$	$Ce_{0.9}Ni_{0.1}O_{2-\delta}$	$Ce_{0.9}Cu_{0.1}O_{2-\delta}$
Ce 3d	**Amount of Ce^{3+} (%)**	33	19	30	28	31	21
	Amount of Ce^{4+} (%)	67	81	70	72	69	79
	Mean Ce valence state	3.67	3.81	3.70	3.72	3.69	3.79
M 2p	**Concentration of transition metal cations (%)**	n/a	Mn^{2+}: 50 Mn^{3+}: 35 Mn^{4+}:15	Fe^{2+}: 60 Fe^{3+}: 40	Co^{2+}: 85 Co^{3+}: 15	Ni^{2+}: 46 Ni^{3+}: 54	Cu^{+}: 91 Cu^{2+}: 9
	Mean valence state of transition metal	n/a	2.66	2.40	2.15	2.54	1.09

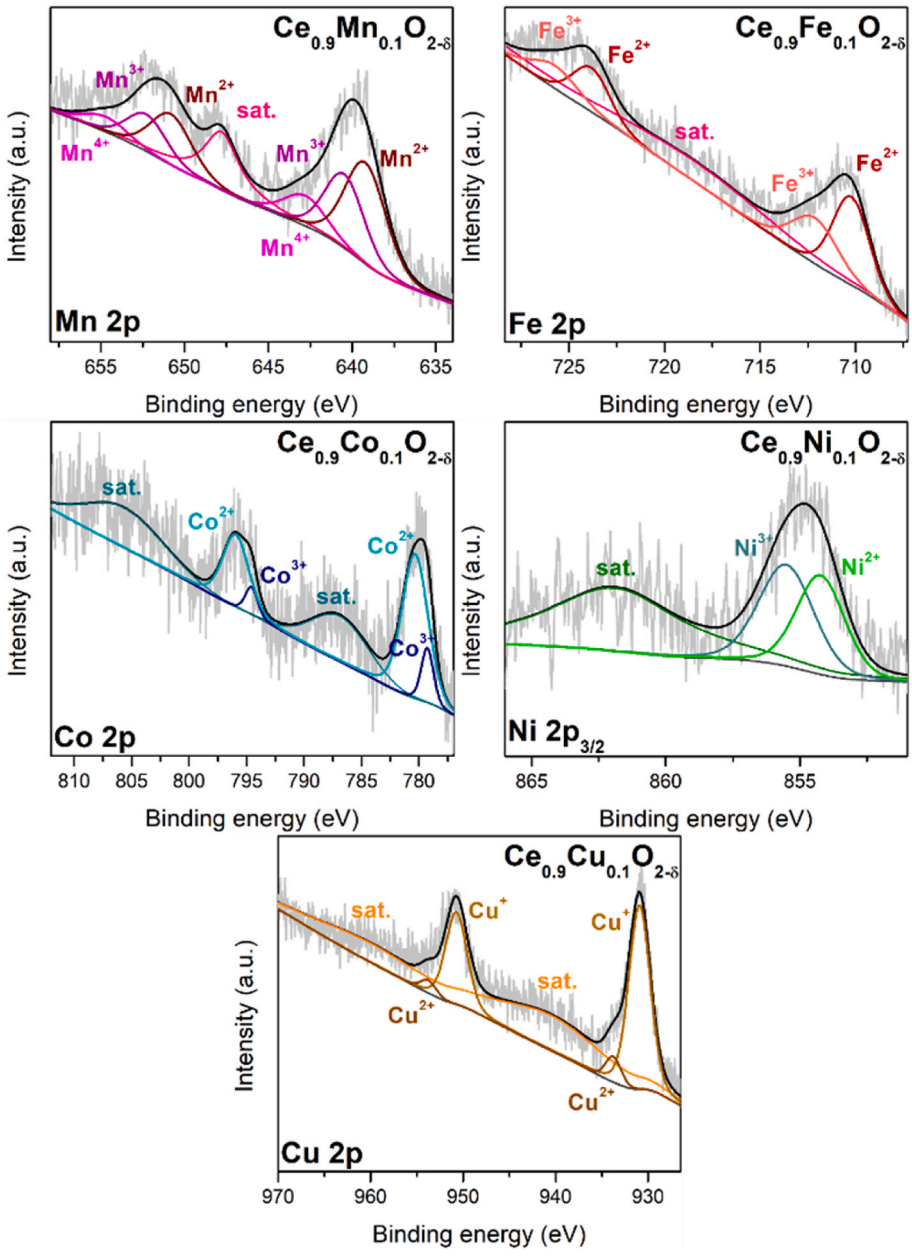

Fig. 6. XPS spectra for respective transition metals in doped cerium (IV) oxide. Abbreviation sat. stands for shake-up satellites.

signal, which was also observed in another article [87], and as a result the characteristic Ni^{3+} peak at around 856 eV is not clearly visible. The formation of both Ni cations agrees with the observation from XPS measurements. Moreover, a similar observation was reported by Derafa et al. [32] who found out that the local environment of incorporated nickel is characterized by trivalent nickel cations, while NiO agglomerates contribute to Ni^{2+} signal. In contrast, after the crystallization, the spectrum was identical to the one obtained for NiO reference. This observation proved the formation of more stable Ni^{2+} ions after additional annealing. Finally, the Cu-doped sample has shown two clearly distinguishable L_3 peaks in its spectrum for as-synthesized powder. The first one located at 931 eV originated from the CuO (Cu^{2+}), while the second one at 934 eV was attributed fully to the Cu^{+}. A relatively high and broad peak from Cu^{+} suggests that this is a predominant phase, which is in line with the XPS studies. Furthermore, after the annealing, the relationship between these two peaks changes, as the amount of Cu^{2+} increases and more CuO is formed. Although the presence of Cu^{+} may result from partial reduction under vacuum (both in XPS and XAS measurement), the changing ratio of Cu^{+}:Cu^{2+} after the annealing is direct proof of the existence of copper in a lower oxidation state in comparison to an as-synthesized sample.

The K-edge of cerium was collected in transmittance mode at the LISA beamline in ESRF, Grenoble, France. The normalized absorption edge for all as-synthesized compounds is presented in Fig. S5, and its shape is comparable to the findings in the literature for pristine CeO_2 obtained by the precipitation method [66]. No significant changes were observed in the shape or position of the Ce-K edge after the doping with different transition metals, meaning that the oxidation state of cerium was not much altered. The EXAFS functions with marked Fourier transform window (k = 3–13 $Å^{-1}$) are presented in Fig. S6. Fig. 8A presents a radial distribution function (RDF) of the Ce K-edges in which two clearly distinguishable peaks are visible. The one at 2.15 Å is the first coordination shell of the Ce and is attributed to Ce-O bonds, while the latter one is the second coordination shell of Ce-Ce bonds and is located at 3.83 Å. Because the energy required to collect the Ce K-edge is out of range of most synchrotrons, most of the literature reports focus on

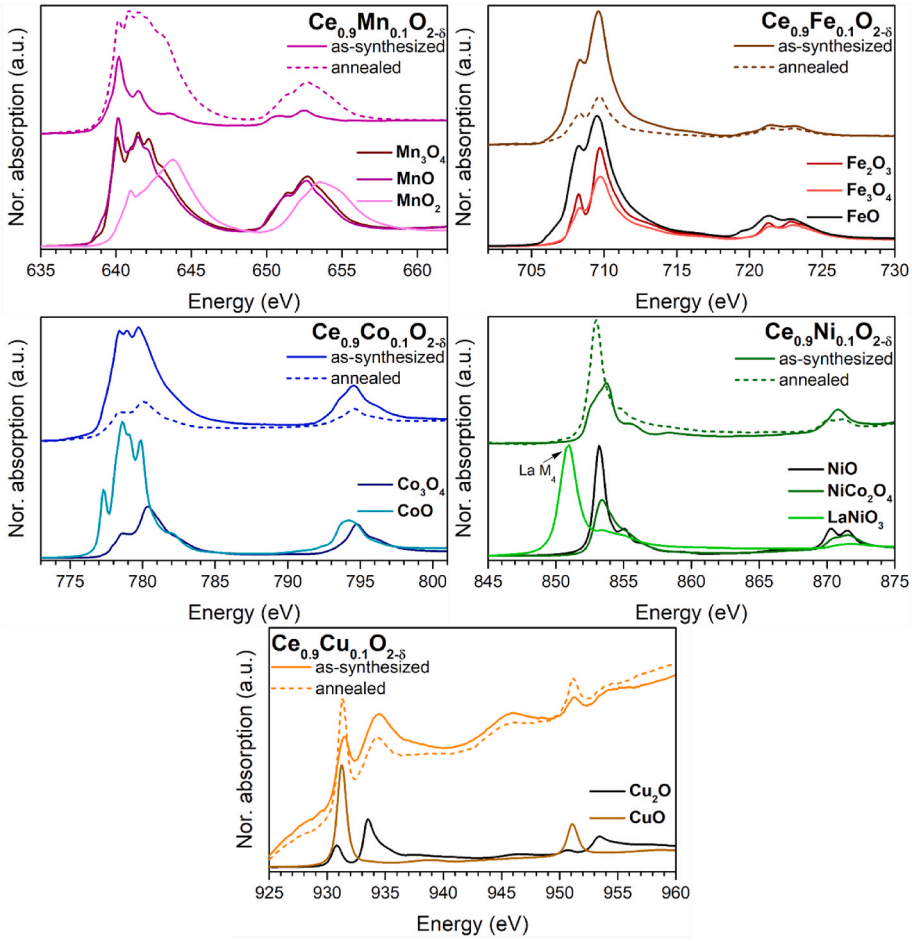

Fig. 7. $L_{3,2}$-edges of respective transition metals for as-synthesized and annealed states in doped ceria.

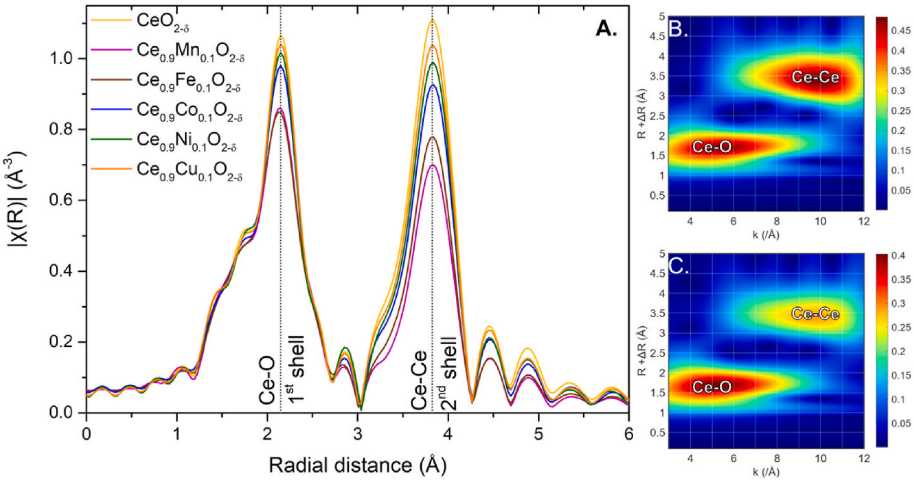

Fig. 8. A. Radial distribution function (RDF) obtained from Fourier Transform of Ce K-edge EXAFS of as-synthesized oxides (with phase correction); B. Wavelet Transform of Ce K-edge of $CeO_{2-\delta}$; C. Wavelet Transform of Ce K-edge of $Ce_{0.9}Mn_{0.1}O_{2-\delta}$.

the Ce $L_{3,2}$ or even $M_{5,4}$ edges, which is further utilized to obtain RDF [63,88,89]. However, Lee et al. [66] have studied the K-edge and also performed Fourier analysis with the fitting of respective shells. They have obtained the same values for the second coordination shell (Ce-Ce) bonds, which is also the expected value from the crystallographic structure. At the same time, the Ce-O bond length obtained from their calculations was around 2.3 Å. Herein, the length is found to be c.a. 0.15 Å smaller than reported in Ref. [66], although the particle size is comparable between this manuscript and the literature. Tiwari et al. [88] explained the shortening of Ce-O bond by the terms of the doping and/or formation of the oxygen vacancies. Furthermore, the intensity of the peaks has changed after the transition metals have been introduced. The changes in the intensity of the RDF peaks indicate changes in the coordination number of Ce ions, where the lower the intensity, the lower

the coordination number. The intensity of both peaks is the lowest for Mn- and Fe-doped ceria, indicating the highest amount of incorporated metal. On the other hand, Cu-doped sample have the highest peak intensity from all doped compounds, meaning that most of the copper ions remained on the surface rather than being dissolved into the cerium oxide. Those two observations prove that most of the manganese ions were incorporated into the ceria host when compared to other dopants. Fig. 8B and C shows the Wavelet transform of pristine ceria and Mn-doped one, respectively. It allowed to visualize the shells simultaneously in k- and R-spaces. The Wavelet Transforms for other samples is presented in Fig. S7. The shell visible in lower wavenumbers is associated with Ce-O bonds in 1st coordination shell, while the one at higher wavenumbers and longer radial distances can be identified as Ce-Ce bonding. Despite doping, no additional shells, which may be contributing from Ce-TM bonds can be found. If the dopants are present at interstitial sites, an additional halo should be visible. Moreover, when a significant amount of dopant would be substituting cerium, the formation of any signal at similar R as Ce-Ce shell, but lower in k should be visible. In presented studies, no such behavior is visible, proving that transition metals were not fully incorporated into the ceria lattice. The combined XAS analysis of $L_{3,2}$ edges of transition metals in both as-prepared and annealed states and analysis of K-edge of Ce is evidence of the presence of separated phases of ceria and respective transition metal oxides.

4. Conclusions

The ceria doped with 10 mol.% of transition metals (Mn, Fe, Co, Ni, Cu) was synthesized by the reverse microemulsion method. The first firing at 500 °C led to the formation of nanocrystalline powder as seen both in diffractograms and SEM images. No clear microstructural differences were visible during the imaging; however, additional analysis in BSE mode revealed the segregation of different phases in the as-synthesized powders. Due to the nanocrystallinity, no additional phases were visible in the diffraction patterns, thus additional annealing at 800 °C was performed. In the aftermath, the materials underwent a crystallization process that revealed the presence of additional transition metal oxides that were not fully incorporated into the lattice. The temperature-programmed reduction performed on as-synthesized powders confirmed the existence of the oxides finely dispersed on the surface of the ceria in addition to the limited formation of the solid solution of Ce-Me-O. Furthermore, the irreproducibility of the reduction profile for two subsequent reduction runs indicated either the redistribution of the transition metal-rich phases or the decomposition of the samples. No significant changes were observed for DSC or FTIR between the samples. The deconvolution of the XPS spectra for the Ce and respective metals revealed the changes in the mean valence state of Ce ions upon doping. The doping increased the mean valence state of Ce twofold: by the formation of oxygen vacancies and the presence of transition metals in lower valence states. The predominant existence of lower valence states of each transition metal was verified by the XPS analysis of 2p spectra and also by comparative studies on the $L_{3,2}$ absorption edges. The Radial Distribution Function from Ce-K edge was obtained and revealed that the doping changed the coordination number of cerium ions, but the distance between each shell was almost not affected. Mn showed the highest level of dissolution into CeO_2 from all transition metals. It was confirmed both by the XRD after the annealing and by the RDF results derived from the K absorption edge of Ce. Cu ions could be described as the hardest metal to incorporate into CeO_2 and most of the Cu_xO_y scale remained on the surface.

In conclusion, 10 mol.% of the transition metal cannot be fully incorporated into CeO_2, in contrast to many findings in the literature relying only on diffraction studies. Nanocrystallinity, although desirable for catalysts, hides the existence of additional phases, thus, to properly identify the composition of the materials, several complemental techniques should be utilized for proper structure verification. Most of the metals are mostly dispersed as the oxides on the surface and only a small amount of the solid solution between CeO_2 and metal is being formed.

CRediT authorship contribution statement

Agata Ducka: Writing – original draft, Visualization, Validation, Methodology, Investigation, Formal analysis, Conceptualization. **Patryk Błaszczak:** Writing – review & editing, Validation, Methodology, Investigation, Conceptualization. **Marcin Zając:** Validation, Resources, Methodology, Investigation. **Adrian Mizera:** Methodology, Investigation. **Francesco d'Acapito:** Resources, Methodology. **Beata Bochentyn:** Writing – review & editing, Supervision, Resources, Project administration, Funding acquisition, Data curation.

Declaration of competing interest

The authors declare that they have no known competing financial interests or personal relationships that could have appeared to influence the work reported in this paper.

Acknowledgements

This work was supported by the National Science Centre, Poland, under grant No. NCN 2021/42/E/ST5/00450. This publication was partially developed under the provision of the Polish Ministry and Higher Education project "Support for research and development with the use of research infrastructure of the National Synchrotron Radiation Centre SOLARIS" under contract nr 1/SOL/2021/2. We acknowledge SOLARIS Centre for the access to the Beamline PIRX, where the measurements were performed. The authors acknowledge the CERIC-ERIC Consortium for the access to experimental facilities and financial support for measurements at European Synchrotron Radiation Facility. The access to ESRF was co-financed by the Polish Ministry of Education and Science – decision number: 2021/WK/11. The authors would like to thank Marcin Łapiński, Marta Prześniak-Welenc, Karolina Milewska, and Jakub Karczewski for XPS, DSC, FTIR, and SEM-BSE measurements, respectively.

Appendix A. Supplementary data

Supplementary data to this article can be found online at https://doi.org/10.1016/j.ceramint.2024.10.004.

References

[1] P.P. Ortega, B. Hangai, H. Moreno, L.S.R. Rocha, M.A. Ramírez, M.A. Ponce, et al., Tuning structural, optical, and gas sensing properties of ceria-based materials by rare-earth doping, J. Alloys Compd. 888 (2021) 161517, https://doi.org/10.1016/j.jallcom.2021.161517.
[2] N. Izu, I. Matsubara, T. Itoh, T. Akamatsu, W. Shin, CO responses of sensors based on cerium oxide thick films prepared from clustered spherical nanoparticles, Sensors 13 (2013) 3252–3261, https://doi.org/10.3390/s130303252.
[3] E.Y. Pikalova, A.N. Demina, A.K. Demin, A.A. Murashkina, V.E. Sopernikov, N. O. Esina, Effect of doping with Co2O3, TiO2, Fe2O3, and Mn2O3 on the properties of Ce0.8Gd0.2O2-δ, Inorg. Mater. 43 (2007) 735–742, https://doi.org/10.1134/S0020168507070126.
[4] S.H. Park, H.I. Yoo, Defect-chemical role of Mn in Gd-doped CeO2, Solid State Ionics 176 (2005) 1485–1490, https://doi.org/10.1016/j.ssi.2005.03.015.
[5] M. Choolaei, Q. Cai, R.C.T. Slade, B. Amini Horri, Nanocrystalline gadolinium-doped ceria (GDC) for SOFCs by an environmentally-friendly single step method, Ceram. Int. 44 (2018) 13286–13292, https://doi.org/10.1016/J.CERAMINT.2018.04.159.
[6] Y.X. Zhang, M. Huang, F. Li, Z.Q. Wen, Controlled synthesis of hierarchical CuO nanostructures for electrochemical capacitor electrodes, Int. J. Electrochem. Sci. 8 (2013) 8645–8661, https://doi.org/10.1016/s1452-3981(23)12916-6.
[7] S. Muduli, T. Ranjan Sahoo, Green synthesis and characterization of CeO2 and Ni-doped CeO2 nanoparticles and its dielectric properties, Mater. Today Proc. 74 (2023) 697–702, https://doi.org/10.1016/j.matpr.2022.10.278.
[8] Y. Gao, S. Teng, Z. Wang, B. Wang, W. Liu, W. Liu, et al., Enhanced catalytic performance of cobalt and iron co-doped ceria catalysts for soot combustion, J. Mater. Sci. 55 (2020) 283–297, https://doi.org/10.1007/s10853-019-03973-z.

[9] Y. Sheng, Y. Zhou, H. Lu, Z. Zhang, Y. Chen, Soot combustion performance and H2-TPR study on ceria-based mixed oxides, Cuihua Xuebao/Chinese J Catal 34 (2013) 567–577, https://doi.org/10.1016/S1872-2067(11)60495-6.

[10] J. Li, G. Lu, G. Wu, D. Mao, Y. Wang, Y. Guo, Promotional role of ceria on cobaltosic oxide catalyst for low-temperature CO oxidation, Catal. Sci. Technol. 2 (2012) 1865–1871, https://doi.org/10.1039/c2cy20118f.

[11] X. Tang, B. Zhang, Y. Li, Y. Xu, Q. Xin, W. Shen, CuO/CeO2 catalysts: redox features and catalytic behaviors, Appl. Catal. Gen. 288 (2005) 116–125, https://doi.org/10.1016/j.apcata.2005.04.024.

[12] G. Avgouropoulos, T. Ioannides, Selective CO oxidation over CuO-CeO2 catalysts prepared via the urea-nitrate combustion method, Appl. Catal. Gen. 244 (2003) 155–167, https://doi.org/10.1016/S0926-860X(02)00558-6.

[13] L. Zhou, X. Li, Z. Yao, Z. Chen, M. Hong, R. Zhu, et al., Transition-metal doped ceria microspheres with nanoporous structures for CO oxidation, Sci. Rep. 6 (2016) 1–7, https://doi.org/10.1038/srep23900.

[14] T. Cwele, N. Mahadevaiah, S. Singh, H.B. Friedrich, Effect of Cu additives on the performance of a cobalt substituted ceria (Ce0.90Co0.10O2–δ) catalyst in total and preferential CO oxidation, Appl. Catal. B Environ. 182 (2016) 1–14, https://doi.org/10.1016/J.APCATB.2015.08.043.

[15] J.S. Elias, K.A. Stoerzinger, W.T. Hong, M. Risch, L. Giordano, A.N. Mansour, et al., In situ spectroscopy and mechanistic insights into CO oxidation on transition-metal-substituted ceria nanoparticles, ACS Catal. 7 (2017) 6843–6857, https://doi.org/10.1021/ACSCATAL.7B01600/SUPPL_FILE/CS7B01600_SI_001.PDF.

[16] H.J. Kim, G. Lee, M.G. Jang, K.J. Noh, J.W. Han, Rational design of transition metal Co-doped ceria catalysts for low-temperature CO oxidation, ChemCatChem 11 (2019) 2288–2296, https://doi.org/10.1002/CCTC.201900178.

[17] K.J. Lee, Y. Kim, J.H. Lee, S.J. Cho, J.H. Kwak, H.R. Moon, Facile synthesis and characterization of nanostructured transition metal/ceria solid solutions (TMxCe1-xO2-δ, TM = Mn, Ni, Co, or Fe) for CO oxidation, Chem. Mater. 29 (2017) 2874–2882, https://doi.org/10.1021/acs.chemmater.6b05098.

[18] P.M. Shah, L.A. Bailey, S.H. Taylor, The influence of cerium to manganese ratio and preparation method on the activity of ceria-manganese mixed metal oxide catalysts for VOC total oxidation, Catalysts 13 (2023), https://doi.org/10.3390/catal13010114.

[19] R. Dziembaj, M. Molenda, L. Chmielarz, M. Drozdek, M.M. Zaitz, B. Dudek, et al., Nanostructured Cu-doped ceria obtained by reverse microemulsion method as catalysts for incineration of selected VOCs, Catal. Lett. 135 (2010) 68–75, https://doi.org/10.1007/s10562-010-0264-9.

[20] R. Dziembaj, M. Molenda, M.M. Zaitz, L. Chmielarz, K. Furczoń, Correlation of electrical properties of nanometric copper-doped ceria materials (Ce1 - XCuxO2 - δ) with their catalytic activity in incineration of VOCs, Solid State Ionics 251 (2013) 18–22, https://doi.org/10.1016/j.ssi.2013.03.011.

[21] L. Liu, J. Shi, X. Zhang, J. Liu, Flower-like Mn-doped CeO2 microstructures: synthesis, characterizations, and catalytic properties, J. Chem. 2015 (2015), https://doi.org/10.1155/2015/254750.

[22] D. Dong, X. Shao, Z. Wang, C. Lievens, J. Yao, H. Wang, et al., Fibrous NiO/CeO2 nanocatalysts for the partial oxidation of methane at microsecond contact times, RSC Adv. 3 (2013) 1341–1345, https://doi.org/10.1039/c2ra21229c.

[23] A.H. Fakeeha, S. Barama, A.A. Ibrahim, R.L. Al-Otaibi, A. Barama, A.E. Abasaeed, et al., In situ regeneration of alumina-supported Cobalt–iron catalysts for hydrogen production by catalytic methane decomposition, Catalysts 8 (2018), https://doi.org/10.3390/catal8110567.

[24] Y. Wei, H. Wang, K. Li, Ce-Fe-O mixed oxide as oxygen carrier for the direct partial oxidation of methane to syngas, J. Rare Earths 28 (2010) 560–565, https://doi.org/10.1016/S1002-0721(09)60154-X.

[25] J. Vecchietti, A. Bonivardi, W. Xu, D. Stacchiola, J.J. Delgado, M. Calatayud, et al., Understanding the role of oxygen vacancies in the water gas shift reaction on ceria-supported platinum catalysts, ACS Catal. 4 (2014) 2088–2096, https://doi.org/10.1021/cs500323u.

[26] Y. Li, M. Kottwitz, J.L. Vincent, M.J. Enright, Z. Liu, L. Zhang, et al., Dynamic structure of active sites in ceria-supported Pt catalysts for the water gas shift reaction, Nat. Commun. 12 (2021) 1–9, https://doi.org/10.1038/s41467-021-21132-4.

[27] K. Yuan, Y. Guo, Q.L. Lin, L. Huang, J.T. Ren, H.C. Liu, et al., Size effect-tuned water gas shift reaction activity and pathway on ceria supported platinum catalysts, J. Catal. 394 (2021) 121–130, https://doi.org/10.1016/j.jcat.2020.12.035.

[28] E.T. Saw, U. Oemar, M.L. Ang, H. Kus, S. Kawi, High-temperature water gas shift reaction on Ni-Cu/CeO2 catalysts: effect of ceria nanocrystal size on carboxylate formation, Catal. Sci. Technol. 6 (2016) 5336–5349, https://doi.org/10.1039/c5cy01932j.

[29] Y. Qi, J. Ye, S. Zhang, Q. Tian, N. Xu, P. Tian, et al., Controllable synthesis of transition metal ion-doped CeO2 micro/nanostructures for improving photocatalytic performance, J. Alloys Compd. 782 (2019) 780–788, https://doi.org/10.1016/j.jallcom.2018.12.111.

[30] M.A.M. Khan, W. Khan, M. Ahamed, A.N. Alhazaa, Microstructural properties and enhanced photocatalytic performance of Zn doped CeO2 nanocrystals, Sci. Rep. 7 (2017) 1–11, https://doi.org/10.1038/s41598-017-11074-7.

[31] R. Verma, S.K. Samdarshi, S. Bojja, S. Paul, B. Choudhury, A novel thermophotocatalyst of mixed-phase cerium oxide (CeO2/Ce2O3) homocomposite nanostructure: role of interface and oxygen vacancies, Sol. Energy Mater. Sol. Cells 141 (2015) 414–422, https://doi.org/10.1016/j.solmat.2015.06.027.

[32] W. Derafa, F. Paloukis, B. Mewafy, W. Baaziz, O. Ersen, C. Petit, et al., Synthesis and characterization of nickel-doped ceria nanoparticles with improved surface reducibility, RSC Adv. 8 (2018) 40712–40719, https://doi.org/10.1039/C8RA07995A.

[33] K.O. Abdulwahab, M.M. Khan, J.R. Jennings, Doped ceria nanomaterials: preparation, properties, and uses, ACS Omega 8 (2023) 30802–30823, https://doi.org/10.1021/acsomega.3c01199.

[34] G.K. Pradhan, K. Parida, Fabrication of iron-cerium mixed oxide: an efficient photocatalyst for dye degradation, Int. J. Eng. Sci. Technol. 2 (2011) 53–65, https://doi.org/10.4314/ijest.v2i8.63780.

[35] I.T. Liu, M.H. Hon, L.G. Teoh, Structure and optical properties of CeO2 nanoparticles synthesized by precipitation, J. Electron. Mater. 42 (2013) 2536–2541, https://doi.org/10.1007/s11664-013-2617-9.

[36] R. Zamiri, S.A. Salehizadeh, H.A. Ahangar, M. Shabani, A. Rebelo, J.M.F. Ferreira, Dielectric and optical properties of Ni- and Fe-doped CeO2 Nanoparticles, Appl. Phys. Mater. Sci. Process 125 (2019) 1–7, https://doi.org/10.1007/s00339-019-2689-3.

[37] A.A. Ansari, J. Labis, M. Alam, S.M. Ramay, N. Ahmad, A. Mahmood, Effect of cobalt doping on structural, optical and redox properties cerium oxide nanoparticles, Phase Transitions 89 (2016) 261–272, https://doi.org/10.1080/01411594.2015.1116532.

[38] X. Wang, J.A. Rodriguez, J.C. Hanson, D. Gamarra, A. Martínez-Arias, M. Fernández-García, Unusual physical and chemical properties of Cu in Ce 1-xCu xO 2 oxides, J. Phys. Chem. B 109 (2005) 19595–19603, https://doi.org/10.1021/jp051970h.

[39] P. Paschalidou, C.R. Theocharis, Surface properties of ceria synthesised using Triton-X based reverse microemulsions, RSC Adv. 9 (2019) 7025–7031, https://doi.org/10.1039/C8RA08947G.

[40] S. Kuharuangrong, Ionic conductivity of Sm, Gd, Dy and Er-doped ceria, J. Power Sources 171 (2007) 506–510, https://doi.org/10.1016/j.jpowsour.2007.05.104.

[41] A.I.Y. Tok, S.W. Du, F.Y.C. Boey, W.K. Chong, Hydrothermal synthesis and characterization of rare earth doped ceria nanoparticles, Mater. Sci. Eng., A 466 (2007) 223–229, https://doi.org/10.1016/j.msea.2007.02.083.

[42] B. Bochentyn, P. Błaszczak, M. Gazda, A. Fuerte, S.F. Wang, P. Jasiński, Investigation of praseodymium and samarium co-doped ceria as an anode catalyst for DIR-SOFC fueled by biogas, Int. J. Hydrogen Energy 45 (2020) 29131–29142, https://doi.org/10.1016/j.ijhydene.2020.07.146.

[43] Z. Tianshu, P. Hing, H. Huang, J. Kilner, Sintering and densification behavior of Mn-doped CeO2, Mater. Sci. Eng. B 83 (2001) 235–241, https://doi.org/10.1016/S0921-5107(01)00534-7.

[44] K. Neuhaus, R. Dolle, H.-D. Wiemhöfer, The effect of transition metal oxide addition on the conductivity of commercially available Gd-doped ceria, J. Electrochem. Soc. 167 (2020) 044507, https://doi.org/10.1149/1945-7111/ab729b.

[45] S. Kurajica, K. Mužina, G. Dražić, G. Matijašić, M. Duplančić, V. Mandić, et al., A Comparative Study of Hydrothermally Derived Mn, Fe, Co, Ni, Cu and Zn Doped Ceria Nanocatalysts, vol. 244, Elsevier Ltd, 2020, https://doi.org/10.1016/J.MATCHEMPHYS.2020.122689.

[46] H. Li, K. Li, H. Wang, X. Zhu, Y. Wei, D. Yan, et al., Soot combustion over Ce 1-x Fe x O 2-δ and CeO 2/Fe 2 O 3 catalysts: roles of solid solution and interfacial interactions in the mixed oxides, Appl. Surf. Sci. 390 (2016) 513–525, https://doi.org/10.1016/j.apsusc.2016.08.122.

[47] J. Saranya, K.S. Ranjith, P. Saravanan, D. Mangalaraj, R.T. Rajendra Kumar, Cobalt-doped cerium oxide nanoparticles: enhanced photocatalytic activity under UV and visible light irradiation, Mater. Sci. Semicond. Process. 26 (2014) 218–224, https://doi.org/10.1016/j.mssp.2014.03.054.

[48] S. Kumar, A.K. Ojha, Ni, Co and Ni-Co codoping induced modification in shape, optical band gap and enhanced photocatalytic activity of CeO2 nanostructures for photodegradation of methylene blue dye under visible light irradiation, RSC Adv. 6 (2016) 8651–8660, https://doi.org/10.1039/c5ra14184b.

[49] P. Bera, K.R. Priolkar, P.R. Sarode, M.S. Hegde, S. Emura, R. Kumashiro, et al., Structural investigation of combustion synthesized Cu/CeO2 catalysts by EXAFS and other physical techniques: formation of a Ce1-xCuxO2-δ solid solution, Chem. Mater. 14 (2002) 3591–3601, https://doi.org/10.1021/CM0201706/ASSET/IMAGES/LARGE/CM0201706F00011.JPEG.

[50] F. Yang, J. Wei, W. Liu, J. Guo, Y. Yang, Copper doped ceria nanospheres: surface defects promoted catalytic activity and a versatile approach, J. Mater. Chem. A 2 (2014) 5662–5667, https://doi.org/10.1039/c3ta15253g.

[51] C.Y. Kang, H. Kusaba, H. Yahiro, K. Sasaki, Y. Teraoka, Preparation, characterization and electrical property of Mn-doped ceria-based oxides, Solid State Ionics 177 (2006) 1799–1802, https://doi.org/10.1016/j.ssi.2006.04.016.

[52] T. Tsoncheva, C. Rosmini, M. Dimitrov, G. Issa, J. Henych, Z. Němečková, et al., Formation of catalytic active sites in hydrothermally obtained binary ceria-iron oxides: composition and preparation effects, ACS Appl. Mater. Interfaces 13 (2021) 1838–1852, https://doi.org/10.1021/acsami.0c16326.

[53] M.O. Mazan, J. Marrero-Jerez, A. Soldati, P. Núñez, S.A. Larrondo, Fe-doped ceria nanopowders synthesized by freeze-drying precursor method for electrocatalytic applications, Int. J. Hydrogen Energy 40 (2015) 3981–3989, https://doi.org/10.1016/j.ijhydene.2015.01.006.

[54] M.U. Rashid, W.M. Ashri, W. Daud, A. Mohidem, M.B. Mohamad, J. Akhtar, et al., Methane dry reforming with CO2 over ceria supported Ni catalyst prepared by reverse microemulsion synthesis, Fuel 317 (2022) 123433, https://doi.org/10.1016/J.FUEL.2022.123433.

[55] B.Z. Matović, D.M. Bučevac, M. Rosić, B.M. Babić, Z.D. Dohcević-Mitrović, M. B. Radović, et al., Synthesis and characterization of Cu-doped ceria nanopowders, Ceram. Int. 37 (2011) 3161–3165, https://doi.org/10.1016/J.CERAMINT.2011.03.078.

[56] L. Sun, B. Yildiz, Solubility limit of Cu and factors governing the reactivity of Cu-CeO 2 assessed from first-principles defect chemistry and thermodynamics, J. Phys. Chem. C 123 (2019) 399–409, https://doi.org/10.1021/acs.jpcc.8b08222.

[57] S. Soni, V.S. Vats, Kumar Sudhish, B. Dalela, M. Mishra, R.S. Meena, et al., Structural, optical and magnetic properties of Fe-doped CeO 2 samples probed using X-ray photoelectron spectroscopy, J. Mater. Sci. Mater. Electron. 29 (2018) 10141–10153, https://doi.org/10.1007/s10854-018-9060-x.
[58] A. Miri, M. Sarani, M. Khatami, Nickel-doped cerium oxide nanoparticles: biosynthesis, cytotoxicity and UV protection studies, RSC Adv. 10 (2020) 3967–3977, https://doi.org/10.1039/c9ra09076b.
[59] G.D. Takalkar, R.R. Bhosale, A. Kumar, F. AlMomani, M. Khraisheh, R.A. Shakoor, et al., Transition metal doped ceria for solar thermochemical fuel production, Sol. Energy 172 (2018) 204–211, https://doi.org/10.1016/j.solener.2018.03.022.
[60] B. Hołówko, P. Błaszczak, M. Chlipała, M. Gazda, S.F. Wang, P. Jasiński, et al., Structural and catalytic properties of ceria layers doped with transition metals for SOFCs fueled by biogas, Int. J. Hydrogen Energy 45 (2020) 12982–12996, https://doi.org/10.1016/j.ijhydene.2020.02.144.
[61] M. Konsolakis, M. Sgourakis, S.A.C. Carabineiro, Surface and redox properties of cobalt-ceria binary oxides: on the effect of Co content and pretreatment conditions, Appl. Surf. Sci. 341 (2015) 48–54, https://doi.org/10.1016/j.apsusc.2015.02.188.
[62] Y. Sun, T. Wu, Z. Bao, J. Moon, Z. Huang, Z. Chen, et al., Defect engineering of ceria nanocrystals for enhanced catalysis via a high-entropy oxide strategy, ACS Cent. Sci. 8 (2022) 1081–1090, https://doi.org/10.1021/acscentsci.2c00340.
[63] S. Kumar, S. Gautam, T.K. Song, K.H. Chae, K.W. Jang, S.S. Kim, Electronic structure study of Co doped CeO2 nanoparticles using X-ray absorption fine structure spectroscopy, J. Alloys Compd. 611 (2014) 329–334, https://doi.org/10.1016/j.jallcom.2014.05.025.
[64] L. Savereide, A. Gosavi, K.E. Hicks, J.M. Notestein, Identifying properties of low-loaded CoOX/CeO2 via X-ray absorption spectroscopy for NO reduction by CO, J. Catal. 381 (2020) 355–362, https://doi.org/10.1016/j.jcat.2019.11.016.
[65] F. D'Acapito, G.O. Lepore, A. Puri, A. Laloni, F. La Manna, E. Dettona, et al., The LISA beamline at ESRF, J. Synchrotron Radiat. 26 (2019) 551–558, https://doi.org/10.1107/S160057751801843X.
[66] J.F. Lee, M.T. Tang, W.C. Shih, R.S. Liu, Ce K-edge EXAFS study of nanocrystalline CeO2, Mater. Res. Bull. 37 (2002) 555–562, https://doi.org/10.1016/S0025-5408(02)00671-2.
[67] G. Avgouropoulos, T. Ioannides, H. Matralis, Influence of the preparation method on the performance of CuO-CeO 2 catalysts for the selective oxidation of CO, Appl. Catal. B Environ. 56 (2005) 87–93, https://doi.org/10.1016/j.apcatb.2004.07.017.
[68] A. Tschope, W. Liu, M. Flytzani-Stephanopoulos, J.Y. Ying, Redox activity of nonstoichiometric cerium oxide-based nanocrystalline catalysts, J. Catal. 157 (1995) 42–50, https://doi.org/10.1006/jcat.1995.1266.
[69] H.J. Avila-Paredes, S. Kim, The effect of segregated transition metal ions on the grain boundary resistivity of gadolinium doped ceria: alteration of the space charge potential, Solid State Ionics 177 (2006) 3075–3080, https://doi.org/10.1016/j.ssi.2006.08.017.
[70] R.D.S. Revised, Effective ionic radii and systematic studies of interatomie distances in halides and chaleogenides, Acta Crystallogr. 32 (1976) 751–767, https://doi.org/10.1023/A:1018927109487.
[71] S. Phoka, P. Laokul, E. Swatsitang, V. Promarak, S. Seraphin, S. Maensiri, Synthesis, structural and optical properties of CeO2 nanoparticles synthesized by a simple polyvinyl pyrrolidone (PVP) solution route, Mater. Chem. Phys. 115 (2009) 423–428, https://doi.org/10.1016/j.matchemphys.2008.12.031.
[72] H.F. Lopez, H. Mendoza, Temperature effects on the crystallization and coarsening of nano-CeO 2 powders, ISRN Nanomater 2013 (2013), https://doi.org/10.1155/2013/208614.
[73] R. Murugan, L. Kashinath, R. Subash, P. Sakthivel, K. Byrappa, S. Rajendran, et al., Pure and alkaline metal ion (Mg, Ca, Sr, Ba) doped cerium oxide nanostructures for photo degradation of methylene blue, Mater. Res. Bull. 97 (2018) 319–325, https://doi.org/10.1016/j.materresbull.2017.09.026.
[74] J. Marrero-Jerez, S. Larrondo, E. Rodríguez-Castellón, P. Núñez, TPR, XRD and XPS characterisation of ceria-based materials synthesized by freeze-drying precursor method, Ceram. Int. 40 (2014) 6807–6814, https://doi.org/10.1016/J.CERAMINT.2013.11.143.
[75] F. Lin, R. Delmelle, T. Vinodkumar, B.M. Reddy, A. Wokaun, I. Alxneit, Correlation between the structural characteristics, oxygen storage capacities and catalytic activities of dual-phase Zn-modified ceria nanocrystals, Catal. Sci. Technol. 5 (2015) 3556–3567, https://doi.org/10.1039/C5CY00351B.
[76] A. Razeghi, A. Khodadadi, H. Ziaei-Azad, Y. Mortazavi, Activity enhancement of Cu-doped ceria by reductive regeneration of CuO-CeO2 catalyst for preferential oxidation of CO in H2-rich streams, Chem. Eng. J. 164 (2010) 214–220, https://doi.org/10.1016/J.CEJ.2010.07.064.
[77] P. Błaszczak, A. Mizera, B. Bochentyn, S.-F. Wang, P. Jasiński, Preparation of methanation catalysts for high temperature SOEC by β-cyclodextrin-assisted impregnation of nano-CeO2 with transition metal oxides, Int. J. Hydrogen Energy (2021), https://doi.org/10.1016/J.IJHYDENE.2021.10.144.
[78] A.A. Ansari, J.P. Labis, M. Alam, S.M. Ramay, N. Ahmad, A. Mahmood, Synthesis, structural and optical properties of Mn-doped ceria nanoparticles: a promising catalytic material, Acta Metall Sin (English Lett 29 (2016) 265–273, https://doi.org/10.1007/s40195-016-0387-0.
[79] A.S. Reddy, C.Y. Chen, C.C. Chen, S.H. Chien, C.J. Lin, K.H. Lin, et al., Synthesis and characterization of Fe/CeO2 catalysts: epoxidation of cyclohexene, J. Mol. Catal. Chem. 318 (2010) 60–67, https://doi.org/10.1016/j.molcata.2009.11.008.
[80] Q. Zhao, N. Xiang, S. Wen, H. Huo, Q. Li, ZIF-67 derived Cu-Co mixed oxides for efficient catalytic oxidation of formaldehyde at low-temperature, Catalysts 13 (2023), https://doi.org/10.3390/catal13010117.
[81] K.K. Babitha, A. Sreedevi, K.P. Priyanka, B. Sabu, T. Varghese, Structural characterization and optical studies of CeO2 nanoparticles synthesized by chemical precipitation, Indian J. Pure Appl. Phys. 53 (2015) 596–603.
[82] A.A. Ansari, Optical and structural properties of sol-gel derived nanostructured CeO2 film, J. Semiconduct. 31 (2010) 530011–530015, https://doi.org/10.1088/1674-4926/31/5/053001.
[83] K.I. Maslakov, Y.A. Teterin, A.J. Popel, A.Y. Teterin, K.E. Ivanov, S.N. Kalmykov, et al., XPS study of ion irradiated and unirradiated CeO 2 bulk and thin film samples, Appl. Surf. Sci. 448 (2018) 154–162, https://doi.org/10.1016/j.apsusc.2018.04.077.
[84] K.I. Maslakov, Y.A. Teterin, M.V. Ryzhkov, A.J. Popel, A.Y. Teterin, K.E. Ivanov, et al., The electronic structure and the nature of the chemical bond in CeO2, Phys. Chem. Chem. Phys. 20 (2018) 16167–16175, https://doi.org/10.1039/c8cp01442f.
[85] R. Dziembaj, A. Chojnacka, Z. Piwowarska, M. Gajewska, M. Świętosławski, S. Górecka, et al., Comparative study of Co-rich and Ce-rich oxide nanocatalysts (CoxCe1−xOy) for low-temperature total oxidation of methanol, Catal. Today 333 (2019) 196–207, https://doi.org/10.1016/j.cattod.2018.03.042.
[86] X. Wu, Q. Liang, D. Weng, J. Fan, R. Ran, Synthesis of CeO2-MnOx mixed oxides and catalytic performance under oxygen-rich condition, Catal. Today 126 (2007) 430–435, https://doi.org/10.1016/j.cattod.2007.06.014.
[87] M. Hepting, D. Li, C.J. Jia, H. Lu, E. Paris, Y. Tseng, et al., Electronic structure of the parent compound of superconducting infinite-layer nickelates, Nat. Mater. 19 (2020) 381–385, https://doi.org/10.1038/s41563-019-0585-z.
[88] S. Tiwari, G. Rathore, N. Patra, A.K. Yadav, D. Bhattacharya, S.N. Jha, et al., Oxygen and cerium defects mediated changes in structural, optical and photoluminescence properties of Ni substituted CeO2, J. Alloys Compd. 782 (2019) 689–698, https://doi.org/10.1016/j.jallcom.2018.12.009.
[89] J. Purans, A. Azens, C.G. Granqvist, X-ray absorption study of Ce-Ti oxide films, Electrochim. Acta 46 (2001) 2055–2058, https://doi.org/10.1016/S0013-4686(01)00415-7.